Liquid phase migration in cemented carbides – Experiments and modelling

Downloaded from: https://research.chalmers.se, 2026-10-12 02:36 UTC

Citation for the original published paper (version of record):
Salmasi, A., Hanif, I., Jonsson, T. et al (2023). Liquid phase migration in cemented carbides – Experiments and modelling. International Journal of Refractory Metals and Hard Materials, 112. http://dx.doi.org/10.1016/j.ijrmhm.2023.106118

N.B. When citing this work, cite the original published paper.

research.chalmers.se offers the possibility of retrieving research publications produced at Chalmers University of Technology. It covers all kind of research output: articles, dissertations, conference papers, reports etc. since 2004. research.chalmers.se is administrated and maintained by Chalmers Library

(article starts on next page)

International Journal of Refractory Metals and Hard Materials 112 (2023) 106118

Contents lists available at ScienceDirect

International Journal of Refractory Metals and Hard Materials

journal homepage: www.elsevier.com/locate/IJRMHM

Liquid phase migration in cemented carbides – Experiments and modelling

Armin Salmasi [a,*], Imran Hanif [b], Torbjörn Jonsson [b], Henrik Larsson [a,*]

[a] Department of Materials Science, Royal Institute of Technology, 114 28 Stockholm, Sweden
[b] Energy and Materials, Department of Chemistry and Chemical Engineering, Chalmers University of Technology, 412 96 Göteborg, Sweden

ARTICLE INFO

Keywords:
Liquid phase sinteirng
Liquid phase migration
Cemented carbides
Simulation
Modelling

ABSTRACT

Liquid phase migration (LPM) and its potential impact on the phenomenon known as cobalt capping in cemented carbides have been investigated through experiments on fully densified, pre-sintered samples and simulations. A model for LPM was developed based on interface energies, grain size, and contiguity, and was implemented and integrated with Thermo-Calc software to make predictions about the final microstructure. The model's predictions, when applied to cases with gradients in grain size and volume fraction of the binder phase, were found to somewhat match experimental observations. Additionally, it was obsereved that LPM can cause a phenomenon resembling cobalt capping due to gradients in carbon activity.

1. Background

Cemented carbides are metallic composites of hard prismatic WC (α phase) grains embedded in a tough, ductile metallic binder matrix (β phase), which is usually Co-based. Cemented carbide inserts are widely used in rock drilling and machining. For these applications, toughness, hardness, and resistance to chemical wear are crucial. These properties mostly depend on the fraction of the β phase and the grain size of the α phase. In plain cemented carbides (WC-Co), the smaller the α grains, the higher the hardness and the wear resistance, and the higher the fraction of the β phase, the higher the toughness and the smaller the wear resistance. Resistance against thermal fatigue and chipping also depends on the balance between the grain size of the α phase and the volume fraction of the β phase (f_β) [1–3].

To develop new grades of cemented carbides, engineering design of a proper combination of the volume fraction of β and grain size of the α phase is necessary. In addition, the performance of cemented carbides can be enhanced by designing in-homogeneous properties that are locally optimised for the operating conditions. In-homogeneous properties can be achieved by thermochemical processes such as gradient sintering and sintering of multiple powder pressing or additive manufacturing.

During solid and liquid state sintering of cemented carbides, transport of materials by diffusion and Liquid Phase Migration (LPM) are the key processes which can be used to create in-homogeneous properties. The theoretical and experimental aspects of diffusion in sintering of cemented carbides is studied extensively in the literature [4–9].

In the liquid phase sintering of cemented carbides, LPM is the bulk motion of the molten binder. When there is no remaining porosity, the driving force of LPM is the gradient in the local integral sum of the energy of $\alpha\alpha$ grain boundaries ($\gamma_{\alpha\alpha}$) and $\alpha\beta$ phase boundaries ($\gamma_{\alpha\beta}$). This energy gradient forces the system toward equilibrium at the minimum of the total free energy.

In LPM, the contribution of interface energies to the system's free energy may create a flux of liquid binder. In addition to the driving force, the LPM flux is proportional to a kinetic factor (I^{LPM}), which is a function of the permeability of the liquid binder in the α phase skeleton and the viscosity of the liquid binder. The viscosity of the molten binder depends on the temperature and the chemical composition of the liquid metal, and the permeability depends on the microstructure and the rigidity of the carbide skeleton, as well as the wetting of $\alpha\alpha$ grain boundaries with the liquid binder.

The LPM driving force is a result of several microscopic phenomena. First, any difference in the f_β results in the difference in the sum of the $\alpha\alpha$ and $\alpha\beta$ surface areas. Second, any difference in the grain size of α, affects the contact area of the $\alpha\alpha$ and $\alpha\beta$ boundaries. Third, any difference in the carbon activity of the system changes $\gamma_{\alpha\beta}$ and $\gamma_{\alpha\alpha}$ [10]. Finally, any combination of the abovementioned gradients results in LPM, and can level out an initial in-homogeneous distribution of the liquid binder or create an inhomogeneous distribution of the liquid binder from an initially homogeneous distribution.

Experimental and theoretical studies of LPM during sintering of cemented carbides has been investigated previously by a number of different groups [11–22]. The experimental measurements of LPM in the

* Corresponding authors.
E-mail addresses: salmasi@kth.se (A. Salmasi), hlarsso@kth.se (H. Larsson).

https://doi.org/10.1016/j.ijrmhm.2023.106118
Received 4 October 2022; Received in revised form 8 January 2023; Accepted 15 January 2023
Available online 25 January 2023
0263-4368/© 2023 The Authors. Published by Elsevier Ltd. This is an open access article under the CC BY license (http://creativecommons.org/licenses/by/4.0/).

literature are usually obtained by sintering of double pressed green bodies. This approach provides a practical empirical understanding of the LPM, but it fails to differentiate between the capillary effect, which happens during the densification of the porous green body, and what happens after the densification step. After densification, during the remaining period of heating, isothermal keeping, and cooling until solidification of the binder, the binder is in a liquid state. During this time, many events, such as grain growth, dissolution, and re-precipitation of the α grains, and some changes in the carbon activity occur. Any of these events forces the LPM. Investigating the effect of these events on the final microstructure is simplified by doing experiments on pre-sintered fully densified samples, which was the approach taken in the present work; this removes the capillary effect due to porosity.

Recent developments in computational physics and materials science have made it possible to calculate difficult-to-measure properties like viscosity, mean distance, grain growth, interfacial energies, thermodynamic and kinetic properties etc. through ab-initio and molecular dynamics and CALPHAD modelling [3,10]. These developments provide an opportunity to look into the underlying physics of LPM and utilise the modelling tools to design new cemented carbide grades.

Following the CALPHAD method and the Integrated Computational Materials Science (ICME) paradigm, this work studied LPM in cemented carbides by experimentation and modelling. In the experimentation phase, pre-sintered fully densified cemented carbides, to eliminate the capillary effect, were coupled and exposed to interrupted heat treatments followed by quenching. Thus, the obtained experimental information revealed the state of the couples in the liquid-solid two-phase region.

Furthermore, to predict and design the final microstructure, a phenomenological model of LPM is developed and implemented in the YAPFI software [23]. In addition to interfacial energies, the presented model is based on well-known properties of the cemented carbide microstructure, such as contiguity, the volume fraction of the binder phase, carbon activity, and grain size. Furthermore, by coupling the model to the Thermo-Calc software [24], access to automated and accurate thermodynamic variables and equilibrium properties such as volume fractions, molar volumes, and chemical potentials was provided.

It is also shown that difficult-to-measure properties such as interfacial energies and the permeability in the α skeleton can be potentially estimated or validated from controlled interrupted heat treatments of pre-sintered fully densified diffusion couples followed by studies of the as-quenched microstructure and modelling.

2. Methods

2.1. Experiment design and materials

Cemented carbide samples of different binder content and grain size were provided in the form of SNUNs, i.e. sintered rectilinear pieces, and drill bits which were cut to rectilinear pieces ($\widetilde{5}$x12x12 mm). The Co-magnetic (CoM) saturation is a measure of the magnetic saturation (MS) of a sintered cemented carbide sample in relation to the MS of pure cobalt with the same weight (see eq. (1)). The CoM can be used to determine how the MS of pure cobalt changes due to the presence of dissolved tungsten. By determining the fraction of W in the Co(FCC), thermodynamic equilibrium calculations can be used to calculate the total W and C content of the cemented carbide sample using the expression given in eq. (2) [25]. The chemical compositions of the samples, including the fraction of cobalt and the calculated fraction of C, are listed in Table 1. To calculate C content, eq. (2) is derived from the correlation factor (S) between CoM/Co and dissolved W in cobalt (FCC) [26], and by using the TCFE9 [27] thermodynamic database. Because the diffusion of W in cobalt (FCC) is frozen at 1000 °C, the equilibrium fraction of W in cobalt (FCC) at this temperature can be used to calculate the C content of the cemented carbide.

Table 1
Chemical composition of cemented carbide samples presented alongside measured *CoM* values which are used to calculate the C fraction.

	CoM	*W*(*Co*)%	*W*(*C*)%	*W*(*W*)%	H_c[kAm^{-1}]
A	9.14	10.0	5.50		7.92
B	10.95	12.0	5.36		7.20
C	11.08	12.0	5.37		8.06
D	14.35	15.0	5.21	Balance	5.00
E	8.95	9.5	5.54		6.45
G	6.20	6.5	5.73		2.85
H	5.55	6.0	5.75		11.10

$$CoM = \frac{MS^{WC-Co}}{MS^{Co}} \tag{1}$$

$$W(FCC, W) = (1 - CoM/Co) \times S \tag{2}$$

In addition, the measured line intercept (Heyn's [28]) and calculated (Fischmeister & Exner [29]) average grain size of samples are presented in section:Results.

In the design of experimental couples, an effort was made to include different combinations of grain sizes, binder fractions, and carbon activity gradients. Heat treatment profiles in the two-phase liquid-solid region are tabulated in Table 2.

All couples were heat treated in a tube furnace under a flowing argon atmosphere. To avoid oxidation of the samples and to maintain contact between the couples, graphite clamps, and crucibles were used (see Fig. 1a).

It was attempted to minimize the contact between graphite and the surface of experimental couples by encapsulating the samples in graphite crucibles to ensure that only the diffusion couples' edges were in contact with graphite. The clamps were in complete contact with the rack face of the samples to study the combination of LPM and the effect of carbon activity at the surface of the samples.

An S-type ceramic protected thermocouple [30] was used to calibrate the furnace thermometer with the temperature of the hot zone. At the end of each heat treatment, the process was interrupted by pushing the graphite clamp or crucible out of the furnace and dropping it in water.

The higher bound of time to melt the binder was estimated by melting slabs of carbon-saturated Co of the same weight as the experimental couples at 1673 K. The Eutectic point of Co—C is at 1594 K. The observed melting time of the slabs was 300 s. The weights of the couples were measured before and after each heat treatment with a $\pm 1 \cdot 10^{-7}$ kg accuracy, and no weight change was observed. The mass of the couples was $\sim 0.02579 \pm 1 \cdot 10^{-5}$ kg.

can you provide the heat treatment time-temperature profiles? What is the melting temperature for the slabs? The melting time of the slabs was 300 s. Does this mean the holding time 300 s at the heat treatment temperature is just to melt the binder?(which could not be simulated by the equilibrium thermodynamics.

After quenching, samples were cut perpendicular to the connecting interface with a diamond cutting disk. Samples were then mounted in conductive resin and polished. Polishing was done for 20 min with a 9 μm diamond suspension and 20 min with a 2 μm. Samples were then cleansed and prepared for EDS analysis.

Table 2
List of experimental couples and heat treatment conditions.

	A-B	A-B	A-B	B-C	D-E	G-H	G-H
Time[s]	300	600	900	600	600	900	2400
T[K]	1693	1693	1693	1693	1673	1673	1673

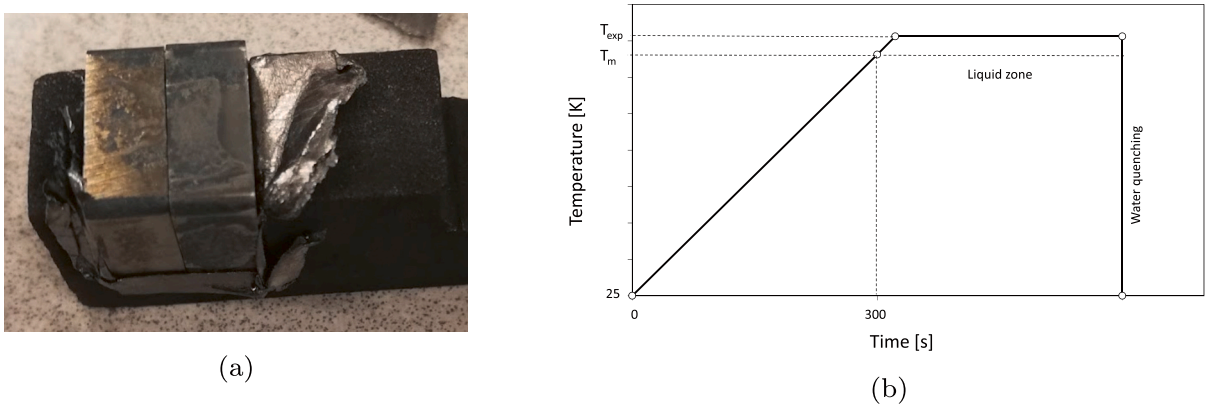

Fig. 1. a) The experimental setup for heat treatment of diffusion couples. b) The schematic heat treatment profile.

2.2. EDS analysis

Energy Dispersive X-ray Spectroscopy (EDS) was used to analyse the chemical composition of samples [31]. Analytical analysis was acquired using the FEI Quanta 3D Scanning Electron Microscope (SEM) equipped with Oxford Instrument's Energy Dispersive X-ray spectroscopy (EDS) detector, and Hitachi S3700N SEM equipped with Bruker QUANTAX X-ray spectrometer.

Before the quantification analysis, EDS analysis was performed on the standard Co samples to measure the beam current and reliability of the EDS data. The quantification was carried out on the test samples by selecting a 180 × 295 μm^2 rectangle by optimizing the processing time and dead time of the detector. The analysis was carried out on different regions of the samples, from the top surface to the bottom. The data was processed using the Oxford Instrument's Aztec software and ESPRIT software by removing the carbon peak and deconvoluting the oxygen peak. Quantification results onto the standard samples were close to the stated composition in The maximum standard deviation of measurements of the raw samples is 0.46 and the maximum mean average error is 0.37.

The results acquired from the test samples indicated the trend of the mass transport and were reproducible. Analysis was performed on the points of a geometrical grid on the cross-section of experimental couples. On each grid point, a probe current of 70 μA was used to map an area of 180x295μm^2 for 300 s.

Since the total mass of experimental couples was conserved after the heat treatment, measured concentrations were adjusted to the initial integral mass of elements. After this, it was possible to compare the integral surfaces averages ($\frac{\iint wt\%Co\, dS}{S}$) of experimental concentrations to the integral line averages ($\frac{\int wt\%Co\, dl}{l}$) of the simulation concentration profiles.

2.3. Phenomenological model

The contribution of the interface energies to the internal energy in a composite material is given by eq. (3).

$$E_V = \sum_{i,j=1}^{N} \gamma_{i,j} \cdot S_{i,j} \left[\mathrm{J\,m^{-3}}\right] \tag{3}$$

In eq. (3), $\gamma_{i,\,j}$ is the energy of interface *i, j* [J m^{-2}] and $S_{i,\,j}$ is the surface area of *i, j* interfaces per unit volume [m^{-1}]. Therefore, the unit of E_V is J m^{-3} which has the same dimension as pressure and stress, $\gamma_{i,\,i}$ represents the grain boundary energy between solid particles of the same phase. In a pore-free two-phase liquid-solid cemented carbide at the liquid phase sintering temperature, the contribution of interface energies to the E_V is the sum of the $\alpha\beta$ phase boundary energy and the $\alpha\alpha$ grain boundary energy, i.e.

$$E_V = \gamma_{\alpha\beta} \cdot S_{\alpha\beta} + \gamma_{\alpha\alpha} \cdot S_{\alpha\alpha} \tag{4}$$

Hence, the contact area between α and β should be known to calculate the total interfacial energy contribution. The contiguity (C) can be used to determine the contact areas from the volume fraction of the binder and grain size. By definition, contiguity is the relative degree of mutual contact between grains of α (eq. (5)).

$$C = \frac{S_{\alpha\alpha}}{S_{\alpha\alpha} + S_{\alpha\beta}} = \frac{S_{\alpha\alpha}}{S_{\alpha}} \tag{5}$$

[*Note: the contiguity is sometimes written as* $C = 2S_{\alpha\alpha}/S_{\alpha}$ *instead of.* $2S_{\alpha\alpha}/(2S_{\alpha\alpha} + S_{\alpha\beta})$ [32]*, but* S_{ij} *is then the number of ij intercepts when the contiguity is estimated from the linear intercept method.]*

Thus, by combining eq. (5) and eq. (3) the interfacial energy per unit volume of the system can be expressed in terms of contiguity, interface energies and the total surface area of α particles (eq. (6)).

$$E_V = \gamma_{\alpha\beta} \cdot S_{\alpha} \cdot (1 - C) + \gamma_{\alpha\alpha} S_{\alpha} \cdot C \tag{6}$$

Contiguity varies in a highly complex manner with the volume fraction of phases (f), the grain size (d), and the grain size distribution (σ). However, multiple authors have derived various relations, some of which are listed in Table 3. By assuming that eq. (6) is valid in both the liquid-solid and the solid regions, and if the changes in phases fractions and grain size of the α grains are known, it is possible to extrapolate any empirical relations of contiguity at solid state to the liquid state.

While it is possible to incorporate any of the mentioned expressions of contiguity into the model, in this work, Stjernberg's [35] expression is used (eq. (7)).

$$C \simeq 1 - \sqrt{1 - f_{\alpha}^2} \tag{7}$$

[*Note:* $f_{\alpha} + f_{\beta} = 1$.]

For cemented carbides, an empirical relation between contiguity, volume fraction, and average grain size of the α phase (Heyn's grain size [28]) can be derived by using Smith & Guttmans [36] postulate on the measurement of internal boundaries in 3D structures by random

Table 3
Empirical expressions relating contiguity to the volume fraction of the binder.

Reference	Contiguity
Roebuck & Bennet [33]	$C = 0.85 - 1.8 f_{\beta}$
Exner & Fischmeister [29]	$C = \frac{0.074}{f_{\beta}}$
Golovchan et al. [34]	$C = 1 - f_{\beta}^{0.644} exp\left(0.391 \left(\frac{\sigma_{\alpha}}{\bar{d}_{\alpha}}\right)\right)$
Stjernberg [35]	$C = 1 - \sqrt{1 - f_{\alpha}^2}$

sectioning of a 2D image (eq. (8)).

$$d_\alpha = \frac{4f_\alpha}{S_\alpha} \tag{8}$$

By combining eqs. (6) to (8), it is trivial to arrive at an expression of E_V as a function of d_α, f_α, $\gamma_{\alpha\alpha}$, and $\gamma_{\alpha\beta}$. By multiplying the result to the molar volume of the system (V_m [m^3 mol^{-1}]) an expression for E_m [J/mol] is obtained

$$E_m = \frac{4f_\alpha}{\overline{d}_\alpha}\left[\gamma_{\alpha\alpha}\left(1-\sqrt{1-f_\alpha^2}\right)+\gamma_{\alpha\beta}\sqrt{1-f_\alpha^2}\right]\cdot V_m \tag{9}$$

Various gradients can be modelled with the analytical expression eq. (9). Grain size, volume fraction and interface energies can be expressed as a function of temperature, time, distance, composition, and any outputs of the Thermo-Calc software equilibrium calculator, e.g. $\gamma_{i,j}$ as a function of carbon activity, $\overline{d}_\alpha$ as a function of time and distance, and f_α as a function of chemical composition or directly from Thermo-Calc output. Thus, under the assumption that the internal friction is sufficient to nullify Newton's first law, the LPM flux is given by

$$J_k = -\Gamma_k^{LPM}\frac{\partial E_m}{\partial z} \tag{10}$$

Here, J_k and Γ_k^{LPM} are molar flux and LPM kinetic coefficient of the multiphase mixture of component k in β, respectively.

In addition to calculating the material transport during LPM another possible application of the phenomenological model is to estimate the permeability κ. Darcy's law for flow of a fluid through a porous medium states that in the absence of gravitational forces and in a homogeneously permeable microstructure, for slow viscous flow, flux of a liquid J_V [m s^{-1}] or J_m [mol m^{-2} s^{-1}] is given by the proportionality between the permeability κ [m^2] of the solid, the dynamic viscosity of the fluid μ [Pas], and the pressure difference over distance (eq. (11)).

$$J_V = -\frac{\kappa}{\mu}\frac{\partial p}{\partial z} \Rightarrow J_m = -\frac{\kappa}{\mu\cdot V_m^2}\frac{\partial E_m}{\partial z} \tag{11}$$

If Darcy's conditions are met in the LPM process, then it is possible to calculate permeability κ by knowing Γ^{LPM} matrix through eq. (12)

$$\kappa = \Gamma^{LPM}\cdot\mu\cdot V_m^2 \tag{12}$$

In the present work the α grain size was allowed to vary with distance, but not with time. It is left for future work to incorporate the grain growth to the model.

2.4. Mass transport model

The LPM was incorporated as an extension of the so-called homogenization model [37,38] as implemented in the YAPFI software [23]. Disregarding, for the moment, the LPM part, the homogenization model allows for multiphase simulations by a coarse-graining – homogenization – approach by assuming that locally, at each numerical grid point, the state is at all times fully equilibrated. Thus, the local phase fractions, phase compositions, chemical potentials, etc. are given by an equilibrium calculation with the local composition, temperature and pressure as equilibrium conditions. The flux of an element k in a lattice-fixed frame of reference is given by

$$J_k = -\Gamma_k^\star\frac{\partial \mu_k^{l.eq}}{\partial z}, \tag{13}$$

where $\Gamma_k^\star$ is an effective kinetic coefficient of the multiphase mixture, and μ_k is the chemical potential of element k. The *l.eq.* embellishment is added to emphasise that a locally equilibrated state is assumed. In a cemented carbide, all long-range mass transport occurs in the binder phase, and $\Gamma_k^\star$ was here taken as

$$\Gamma_k^\star = f^\beta c_k^\beta M_k^\beta = f^\beta\frac{x_k^\beta}{V_m}M_k^\beta = f^\beta\frac{u_k^\beta}{V_S}M_k^\beta \tag{14}$$

where f^β is the volume fraction β, c_k^β, x_k^β and u_k^β are the concentration, mole fraction and u-fraction of element k in β, respectively. The u-fraction [39] is obtained from the mole fraction as

$$u_k = \frac{x_k}{\sum_{j\in S}x_j} \tag{15}$$

where $j \in S$ means that the summation should only be taken over the substitutional elements. The partial molar volume is assumed to be zero for interstitial elements and constant and equal to V_S for all substitutional elements. In the present work, carbon is taken as an interstitial element and cobalt and tungsten as substitutional. Using the u-fractions allows the fluxes J_k evaluated in a lattice-fixed frame of reference to be transformed to fluxes J_k' in a volume-fixed frame of reference by the following expression [39].

$$J_k^{'} = J_k - u_k\sum_{j\in S}J_j \tag{16}$$

The J_k' fluxes are then combined with the equation of continuity.

$$\frac{\partial c_k}{\partial t} = \frac{\partial}{\partial z}\left(-J_k^{'}\right) \tag{17}$$

The LPM was incorporated by adding a second term to J_k, viz.

$$J_k = -\Gamma_k^\star\frac{\partial \mu_k^{l.eq}}{\partial z} - \Gamma_k^{LPM}\frac{\partial E_m}{\partial z} \tag{18}$$

2.5. Model parameters

2.5.1. Interface energies

Atomic-scale modelling of interfaces in cemented carbides and the effect from local chemistry is extensively studied in [10], where models of interfaces were created based on experimental observations of grain orientations and local chemical composition at the interfaces was taken into account by substitution of interface atoms. In addition, the effect of temperature was evaluated based on the study of temperature-dependent interface energies in cemented carbides. A summary of calculated interface energies at T_m^{Co} + 100 K are presented in Fig. 2 and were used for the modelling of the LPM in this work.

2.5.2. Grain size

The most accurate way of measuring the grain size, orientation, and size distribution is the Electron Backscatter Diffraction (EBSD) analysis. However, sample preparation, measurement, and data analysis of EBSD are time-consuming. Therefore, we used simple qualitative grain size measurement methods in this case study. It is worth mentioning that if the EBSD data is available, it is straightforward to couple it to the model. Other, common methods of measuring $\overline{d}_\alpha$ are the Heyn's [28] linear intercept method (eq. (19)), and the Fischmeister & Exner [29] method based on the coercivity (H_c) and f_α (eq. (20)).

$$\overline{d}_\alpha = \frac{L}{N}\cdot f_\alpha \tag{19}$$

In eq. (19), L is the total length of random intersecting lines, and N is the number of intercepted α grains. Heyn's method is destructive and needs cutting of the sample for imaging.

$$d_\alpha = \frac{5.81}{Hc}\cdot(1-C)\cdot\frac{1-f_\beta}{f_\beta}\ [\mu m] \tag{20}$$

In eq. (20), H_c [kA m^{-1}] is the coercivity, C is the contiguity and f_β the volume fraction of the binder phase. Coupling any of the expressions in Table 3 to eq. (20) gives a relationship between f_β and H_c to $\overline{d}_\alpha$. Using Stjernberg's [35] relation for the contiguity, results in eq. (21).

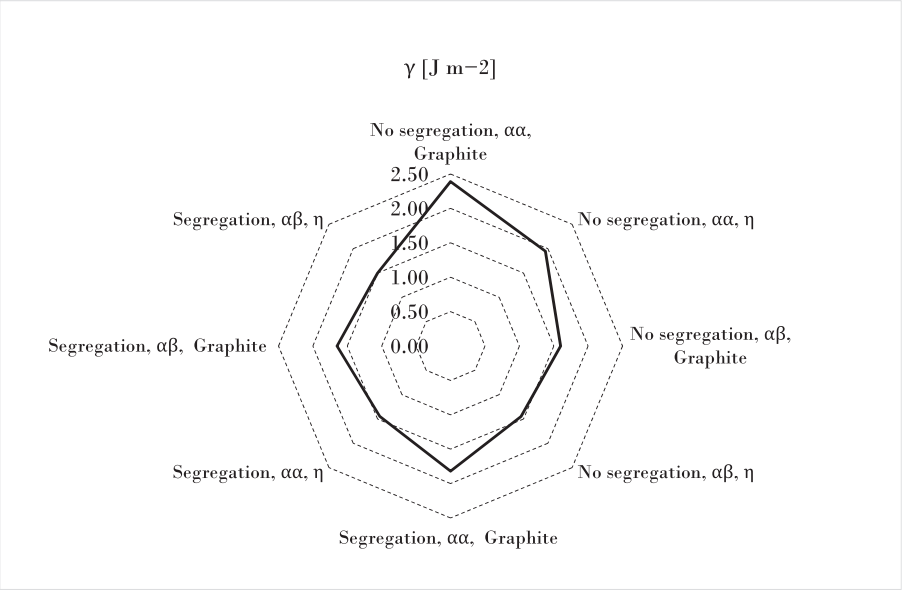

Fig. 2. Interface energies (γ) [J m^{-2}] at $T_m^{Co} + 100K$ after Gren et al. [10].

$$d_\alpha = \frac{5.81}{Hc} \cdot \left(\sqrt{1 - f_\alpha^2}\right) \cdot \frac{f_\alpha}{1 - f_\alpha} \, [\mu m] \tag{21}$$

In eq. (21), if the chemical composition of the cemented carbide is known, the calculation of f_α with computational thermodynamic tools such as Thermo-Calc software is trivial. Since the measurement of H_c is a non-destructive method, eq. (21) represents a non-destructive way of evaluation of the $\overline{d}_\alpha$. In Fig. 3, results of measurement of $\overline{d}_\alpha$ with both aforementioned methods are listed.

All samples used in this work were first sintered in a standard sintering cycle, after which the grain size was evaluated. However, during the heat treatment of couples, α grains dissolve in the liquid binder and the grain size decreases. Assuming that grains are prismatic and the size distribution is narrow, differentiation of smith & Guttman function (eq. (8)) can be used to estimate the shrinkage (eq. (22)).

$$\Delta d = \frac{\Delta f_\alpha}{\frac{\partial V}{\partial d}\big|_{d_0}} = \frac{\Delta f_\alpha}{8 d_0^2} \tag{22}$$

In this work eqs. (21) and (22) were used to estimate the input $\overline{d}_\alpha$ of the models.

2.5.3. Volume fractions and molar volume

The model implementation allows the volume fractions and molar volumes to be obtained from the equilibrium calculator of the Thermo-Calc software by Thermo-Calc Software TCFE Steels/Fe-alloys thermodynamic database version 9 [27].

2.5.4. Boundary conditions

In the simulations of the A-B and B—C couples, a boundary condition for carbon was set corresponding to equilibrium with graphite to

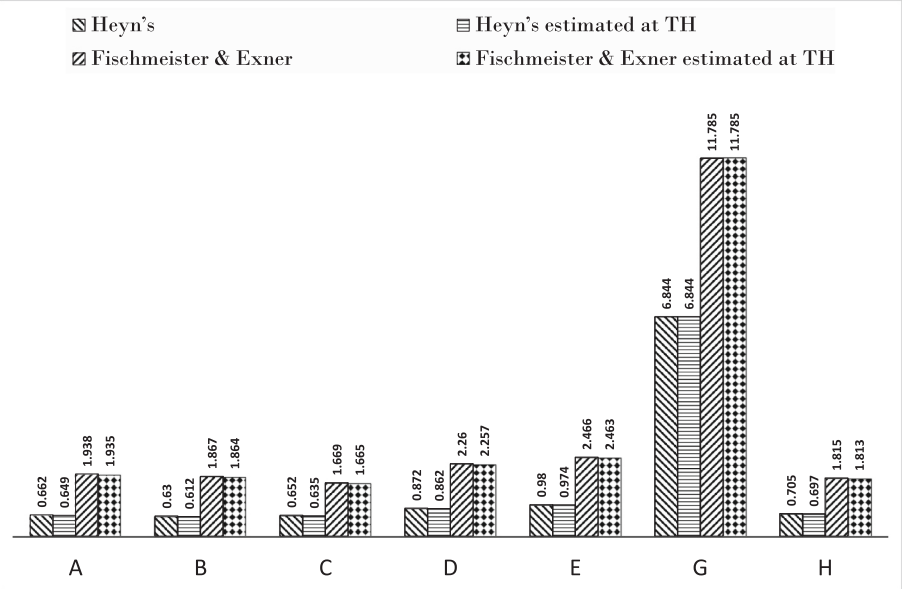

Fig. 3. Measured $\overline{d}_\alpha$ with the Heyn's [28] method and the Fischmeister & Exner [29] method, and estimated grain size at the heat treatment temperatures (TH) of experimental couples in the two-phase liquid-solid region.

account for the contact of the rack faces of the couples with the graphite clamps. A closed boundary condition was used for carbon in the simulation of the D-E and G-H couples. In all simulations, closed boundary conditions were used for cobalt and tungsten.

3. Results

In this section, the results of the interrupted heat treatments of experimental couples are presented. Results include EDS analysis of the grid points on the cross sections of the couples and measured grain sizes of the original pre-sintered fully densified samples. In addition, LPM simulation results are presented and compared to the measured concentration profiles of Co.

3.1. Grain size

The measured grain sizes of the pre-sintered fully densified samples and the estimated grain size at the heat treatment temperatures are presented in Fig. 3.

3.2. EDS measurement of chemical compositions

3D representations of EDS measurements of the Co concentration on cross sections of heat-treated cemented carbide couples are shown in Fig. 4.

The plots are from heat treatment cycles of the A-B cemented carbide couples for 5, 10,and 15 min are shown in Figs. 4a to 4c, respectively. In all plots, the high Co concentration at the surface and the deep concentration of Co in the middle of the couples are observable.

The measured Co concentration profile of the B—C couple, after 10 min of heat treatment, is shown in Fig. 4d. Enrichment of cobalt at the surfaces and minima in the concentration of Co in the middle of the sample is visible in Fig. 4d.

The measured Co concentration profile of the D-E couple, after 10 min of heat treatment, is shown in Fig. 4e. The composition profile agrees with the expectations from the LPM process. The Co enrichment at the surface is not observed in this sample.

The measured Co concentration profile of the G-H couple, after 40 min of heat treatment, is shown in Fig. 4f. The Co enrichment at the surface is not observed in this sample.

3.3. Simulation results

Simulated wt%Co profiles of interrupted heat treatments of the A-B, B—C, D-E and G-H couples are presented in this section along with the simulated profile of wt%Co to the steady state. In addition, the 2D projection of the measured Co concentration profiles are added to the plots for comparison (diamond markers and error bars in red). The error bars show the maximum and minimum Co concentration along the grid lines perpendicular to the axis of the cross-section, and diamond markers show the mean of grid lines. The orange line is the simulated wt %Co profile. The blue line is the initial wt%Co profile. The green dotted line is the integral line average of the simulated profile of wt%Co, and the purple dotted line is the integral surface average of the experimental profile of wt%Co measured on the cross-section of the couple. For comparison to experiments, the red diamond markers are the mean of the experimental profile of wt%Co measured on lines perpendicular to the axis of the couple, and the red error bars are the minimum and maximum of those measurements.

Simulation results of LPM and the effect of carbon activity on the surface of A-B couples for 5, 10, and 15 min of heat treatment are shown in Figs. 5a to 5c. Results of simulating the steady state are presented in Fig. 5d.

Simulation results of LPM and the effect of carbon activity on the surface of the B—C couple for 10-min heat treatment are shown in Fig. 7a. The results obtained by running the simulation to the steady state are presented in Fig. 7b.

Simulation result of LPM of D-E couple for 10 min heat treatment is shown in Fig. 8a. Results of running the simulation to the steady state are presented in Fig. 8b.

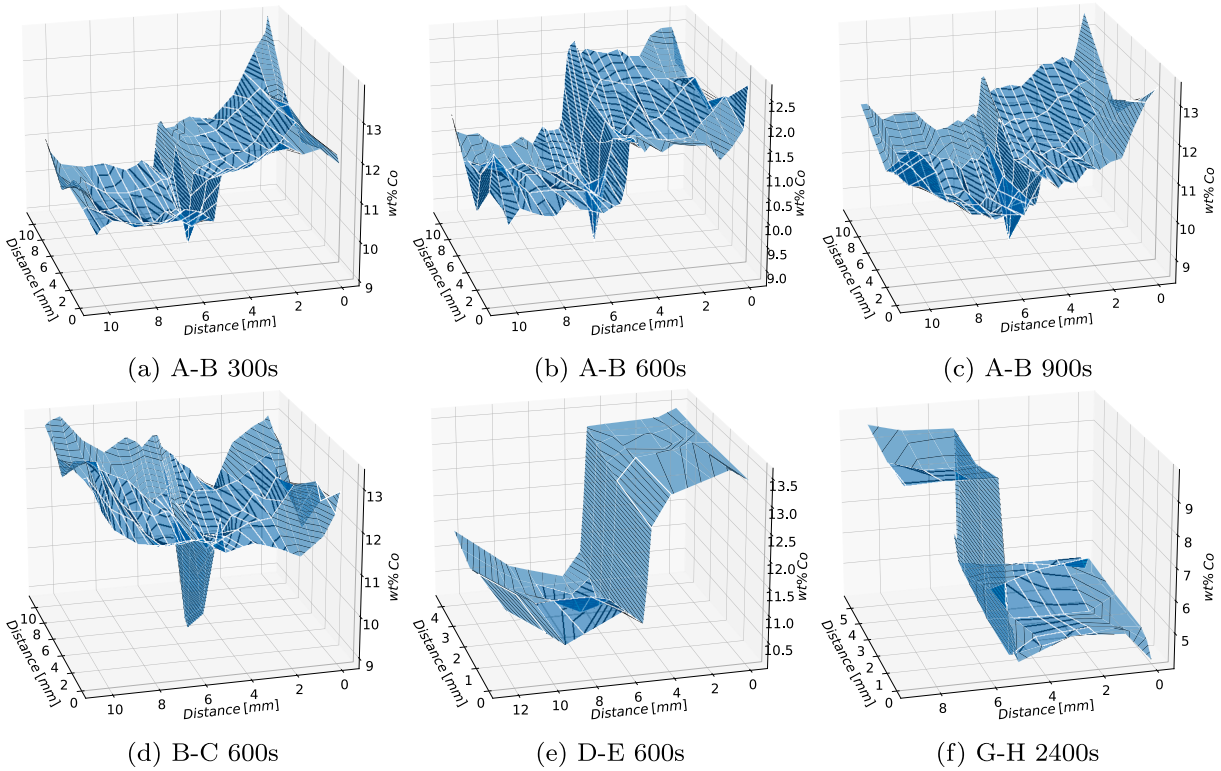

Fig. 4. 3D Co concentration profile of cross sections of heat treated cemented carbide couples measured with EDS.

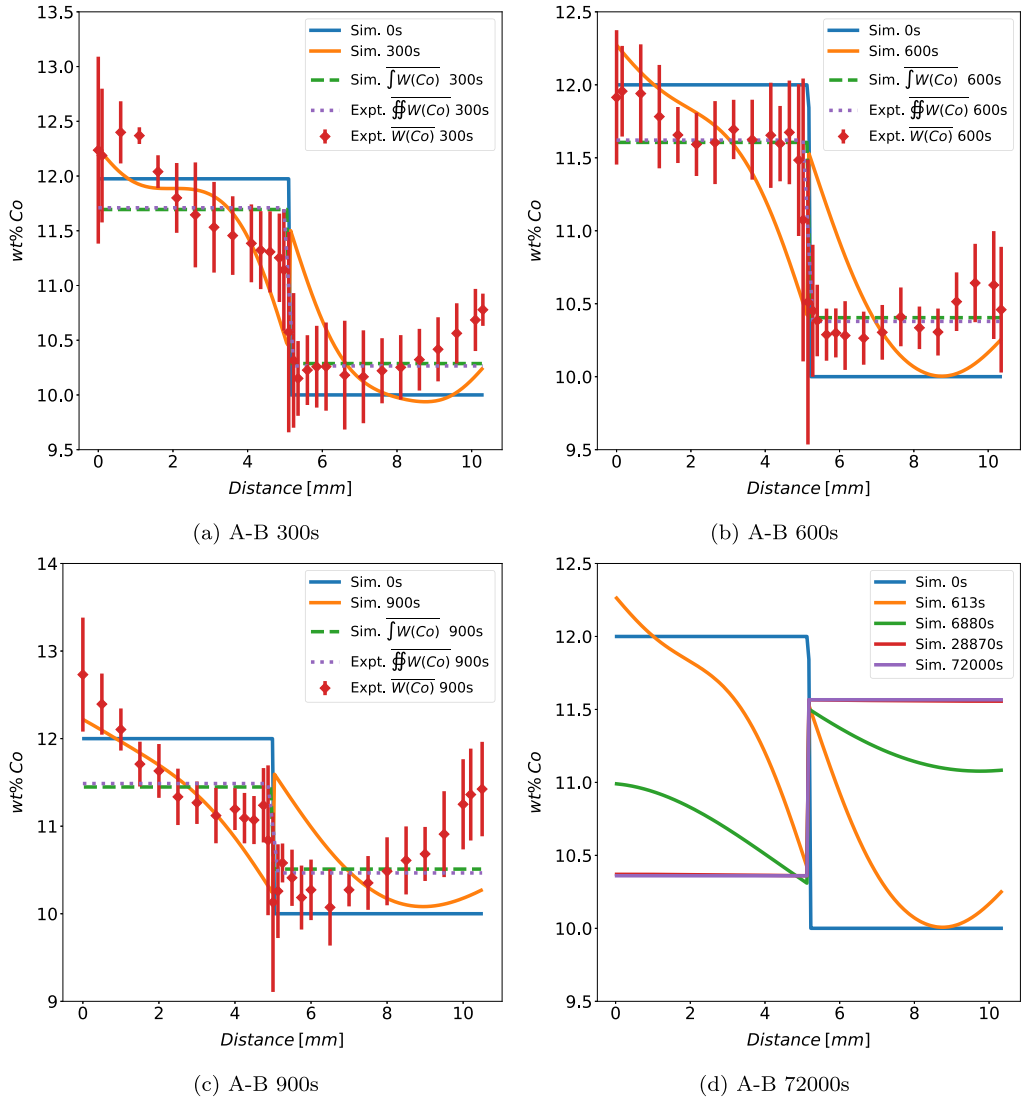

(a) A-B 300s (b) A-B 600s

(c) A-B 900s (d) A-B 72000s

Fig. 5. Simulated Co concentration profiles of A-B couples for 5, 10 and 15 min heat treatment, and 20 h heat treatment at 1693 K.

Simulation results of LPM of G-H couples for 40 min of heat treatment are shown in Fig. 9a. Results of simulating steady state are presented in Fig. 9b.

The kinetic factors Γ^{LPM} which are used in simulations, are tabulated in Table 4.

4. Discussion

The results of the experimental study and the simulations of LPM including the effect of carbon activity on the surface were presented in section 3. In couples, A-B and B—C where the rack faces were in direct contact with the graphite clamp an enrichment in Co content at the surface (Figs. 4a to 4d) which resembles the so-called cobalt capping

Table 4
Applied Γ^{LPM}, temperatures, interface energies and simulation times.

	Time [s]	Γ^{LPM}	$\gamma_{\alpha\alpha}$ [J m^{-2}s]	$\gamma_{\alpha\beta}$ [J m^{-2}s]	T[K]
A-B	300	7×10^{-15}	$8 \times ac(C) + 1.46$	$3.25 \times ac(C) + 1.34$	1693
A-B	600	7×10^{-15}	$8 \times ac(C) + 1.46$	$3.25 \times ac(C) + 1.34$	1693
A-B	900	6×10^{-15}	$8 \times ac(C) + 1.46$	$3.25 \times ac(C) + 1.34$	1693
B-C	600	2×10^{-15}	$8 \times ac(C) + 1.46$	$3.25 \times ac(C) + 1.34$	1693
D-E	600	30×10^{-15}	1.9	1.5	1673
G-H	2400	30×10^{-15}	1.9	1.5	1673

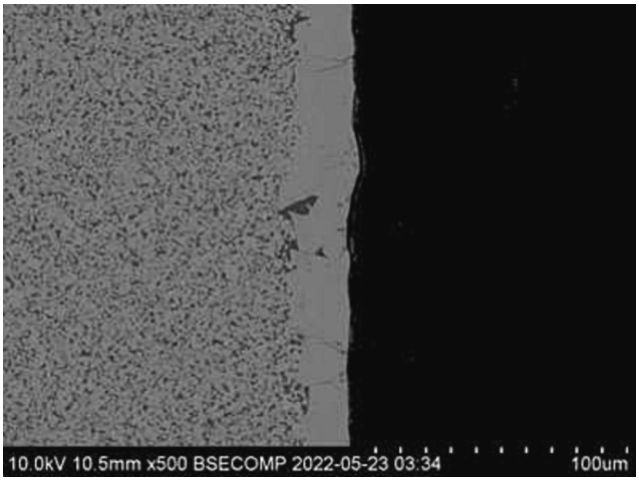

Fig. 6. Cobalt enrichment at the surface of sample A-B 300 s resembles the co-capping phenomenon.

(Co-capping) phenomenon (see Fig. 6) was observed. Co-capping results in the formation of a thin cobalt layer on top of cemented carbides [40]. With regard to the formation of the Co-rich layer, the heat treatment cycle is the most important difference between experiments n this work and previous studies where cemented carbides went through a standard sintering cycle [40,41]. In this work, the samples were in the liquid state for a short time and quenched after heat treatment. Since the microstructure of the initial samples A, B, and C were homogeneous, it seems that the formation of the enriched Co layer at the surface in such a short time cannot be explained by diffusion or abnormalities in the cooling step.

Simulating the LPM process of the A-B and B—C couples with carbon boundary conditions set to equilibrium corresponding to the activity of graphite and allowing the interfacial energy to be a function of carbon activity can answer the underlying cause of the observation. Simulated Co concentration profiles of the A-B and B—C couples (Figs. 5 and 7) show the same enrichment of Co at the surface while the effect of the gradient of volume fraction binder and grain size is visible at the center of the couple. From experimental observations and simulation results, it can be inferred that high carbon activity at the surface changes the interface energies and create a driving force for the migration of the binder toward the surface. The absence of Co-capping in couples D-E and G-H, which were not in direct contact with graphite, strengthen the conclusion. The simulated Co concentration profile in the A-B, B—C, D-E, and G-H couples follow the same trend as the experimentally observed profile, but there is a discrepancy in the magnitude of the profiles.

It should be noted that the surface Co enrichment which resembles the Co-capping, is in conflict with the studies which show that liquid-Co tends to migrate from regions with higher C content to regions with lower C content. Since the argon atmosphere was similar in all experiments, it seems that, if the effect is rooted in the composition of the atmosphere, then the enrichment should be observed in all diffusion couples. However, this phenomenon was only seen in samples that were in direct contact with graphite. Two differences that can possibly explain the inconsistency are, 1) previous experimental observations of Co migrating were from the sintering of green bodies. 2) quenching of diffusion couples was not tried before and samples were cooled slowly in the furnace. In the presented model in this work, the carbon activity affects LPM in diffusion couples of fully sintered samples in two different ways, first, WC grain shape tends to be more round at higher carbon activity, and second, the energy of WC-liquid Co grain boundary is dependent on the C activity [10]. However, it should be pointed out that there may be other driving forces for Co-capping that the present model does not take into account (e.g. volume changes during solidification).

In addition to the Co enrichment at the surface, in the A-B couples the simulated and experimentally obtained profiles for 5, 10, and 15 min (Figs. 5a to 5c), show a dip and a peak in the center which is due to the sharp gradient in the grain size which results in a depletion on the left-hand side of cobalt and an enrichment on the right-hand side. It seems that compared to the overall movement of the binder from left to right because of the gradient in the volume fraction, the effect of grain size is local to the interface between samples. However, in Fig. 5d, the profile obtained for long-time simulations show different behavior. At longer times, the effect of carbon activity on the surface diminishes, which can be because of the saturation of the sample. Since the carbon activity of the samples is below that of graphite, the carbon concentration does not exceed the value corresponding to the carbon activity of the boundary conditions, and the gradient in the interfacial energy eventually levels out. Therefore, the final profile at the steady state is under the influence of the gradient in the grain size only, i.e. the final profile of the volume fraction holds steady indefinitely if there are no further changes in the grain size since. In reality, grain growth will upset this equilibrium.

For the B—C couple, the LPM driving force is created by the carbon activity boundary conditions and the gradient in grain size. As for the A-B couples, in the short term, the grain size gradient has a local effect close to the interface. In the long term, on the other hand, the effect of the carbon activity gradient fades, and the final concentration profile is representative of the minimum free energy. The D-E and G-H samples' simulated and experimental concentration profiles show the expected trend. Nevertheless, the kinetic factor to fit the simulations to the experimental profiles is three times larger than that of the B—C and A-B couples. The difference can be because of the temperature dependency of Γ_k^{LPM} in the form of an inverse Arrhenius expression in eq. (23).

$$\Gamma^{LPM} = 7.659{\cdot}10^{9} \times exp\left(\frac{-35.7{\cdot}10^{5}}{R{\cdot}T}\right) \tag{23}$$

The applied interface energies are calculated with ab-initio methods and molecular dynamics. The accuracy and precision of such calculations depend on the underlying assumptions and used potentials. Since measurement of interface energy at the sintering temperature is difficult, if not impossible, the difference between calculated values and tangible energy of interfaces is a source of error.

Another possibility is that the expression used to relate the contiguity to grain size and volume fraction or to simplify the grain size and distribution to $\overline{d}_{\alpha}$ introduces an error in the calculations. It has been shown

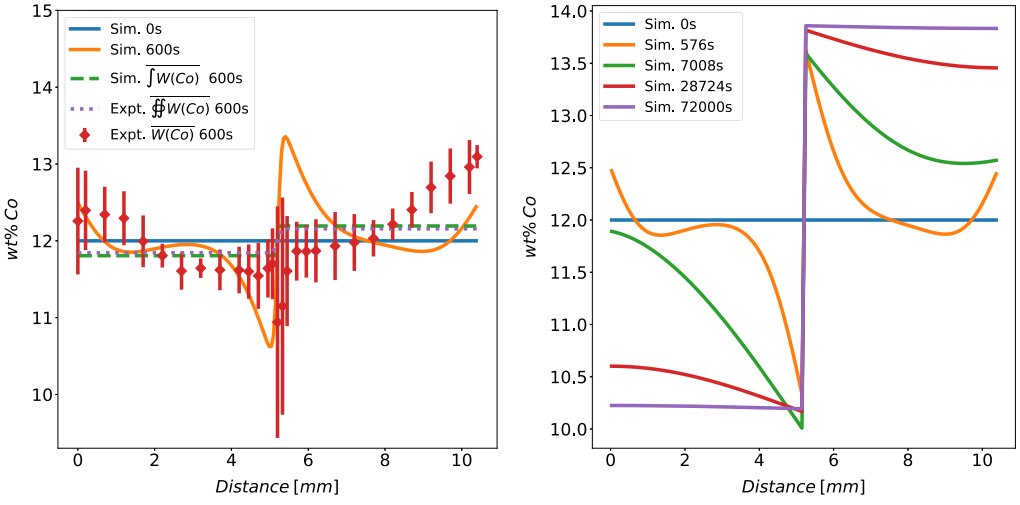

(a) B-C 600s (b) B-C 72000s

Fig. 7. Simulated Co concentration profiles of the B—C couple for 10 min heat treatment, and 20 h heat treatment at 1693 K.

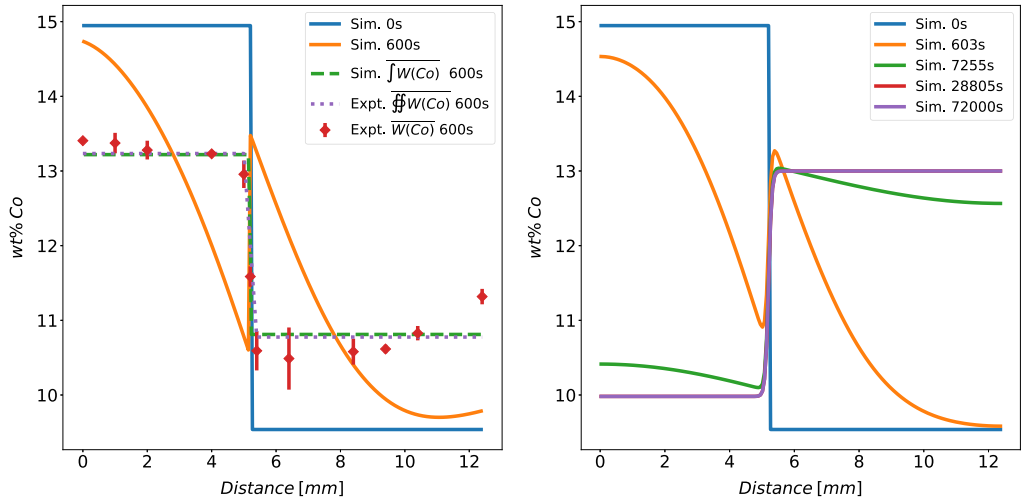

(a) D-E 600s (b) D-E 72000s

Fig. 8. Simulated Co concentration profile of the D-E couple for 10 min heat treatment, and 20 h heat treatment at 1673 K.

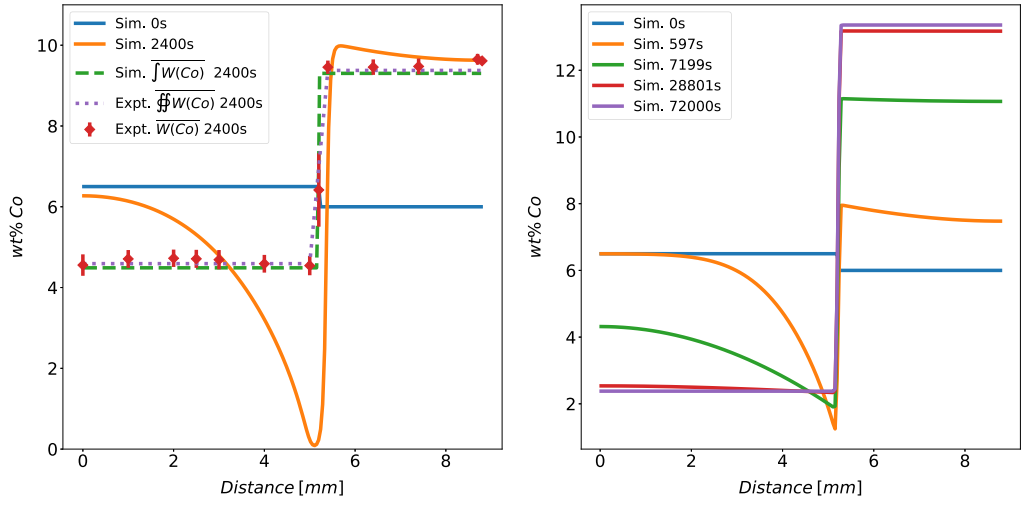

(a) G-H 2400s (b) G-H 72000s

Fig. 9. Simulated Co concentration profile of the G-H couple for 40 min heat treatment, and 20 h heat treatment at 1673 K.

that for $\overline{d}_\alpha < 3$ μm the expression due to Roebuck & Bennet [33] gives a better estimation of the contiguity while for $\overline{d}_\alpha > 3$ μm Stjernberg's expression [35] is more accurate [42].

If the grain size and distribution and expression for contiguity are accurate, a Γ^{LPM} following an Arrhenius behavior is an indicator of the precision of the interfacial energies. On a final note, there is a fair agreement between the experimental observations and the simulation results. Hence, the presented phenomenological model can explain LPM and Co-capping in cemented carbides with some limitations. However, more accurate models of the microstructural properties can be used to enhance the quantitative predictions of the model.

Declaration of Competing Interest

The authors declare the following financial interests/personal relationships which may be considered as potential competing interests:

Armin Salmasi reports financial support was provided by Swedish Foundation for Strategic Research.

Data availability

Data will be made available on request.

Acknowledgment

We would like to dedicate this article to Andreas (Anden) Blomqvist, who unfortunately passed away before the work was completed, but who rightfully should have been a co-author of this paper.

This project was funded by the Swedish Foundation for Strategic Research (SSF), contract RMA15-0062. We would like to acknowledge the support of Sandvik Coromant, Sandvik Mining and Rock Technology, and Seco Tools.

We are grateful to Leif Åkesson (Sandvik Mining and Rock Technology) for providing material and valuable discussions. We would also like to thank Stefan Olovjö (Seco Tools) and Tomas Person (formerly at Seco Tools) for supplying material for this work. We are appreciative of Susanne Norgren for her valuable insights on the magnetic properties of cemented carbides.

References

[1] José García, Veronica Collado Cipres, Andreas Blomqvist, Bartek Kaplan, Cemented carbide microstructures: a review, Int. J. Refract. Met. Hard Mater. 80 (2019) 40–68.

[2] Erik Holmström, Raquel Lizárraga, David Linder, Armin Salmasi, Wei Wang, Bartek Kaplan, Huahai Mao, Henrik Larsson, Levente Vitos, High entropy alloys: substituting for cobalt in cutting edge technology, Appl. Mater. Today 12 (2018) 322–329.

[3] S. Norgren, J. García, A. Blomqvist, L. Yin, Trends in the p/m hard metal industry, Int. J. Refract. Met. Hard Mater. 48 (2015) 31–45.

[4] Armin Salmasi, Simulation of gradient formation in cemented carbides. Master's thesis, Department of materials science and engineering, School of industrial engineering and management, KTH royal intitute of technology, 2016.

[5] Armin Salmasi, Andreas Blomqvist, Henrik Larsson, Geometry effects during sintering of graded cemented carbides: modelling of microstructural evolution and mechanical properties, Results Mater. 1 (2019), 100008.

[6] Martin Walbrühl, Diffusion in the liquid Co binder of cemented carbides: Ab initio molecular dynamics and DICTRA simulations, PhD thesis, Department of materials science and engineering, School of industrial engineering and management, KTH royal intitute of technology, 2014.

[7] Martin Walbrühl, Andreas Blomqvist, Pavel A. Korzhavyi, C. Moyses Araujo, Surface gradients in cemented carbides from first-principles-based multiscale modeling: Atomic diffusion in liquid co, Int. J. Refract. Met. Hard Mater. 66 (2017) 174–179.

[8] José García, Greta Lindwall, Orlando Prat, Karin Frisk, Kinetics of formation of graded layers on cemented carbides: experimental investigations and dictra simulations, Int. J. Refract. Met. Hard Mater. 29 (2) (2011) 256–259.

[9] R. Frykholm, M. Ekroth, B. Jansson, H.-O. Andrén, John Ågren, Effect of cubic phase composition on gradient zone formation in cemented carbides, Int. J. Refract. Met. Hard Mater. 19 (4–6) (2001) 527–538.

[10] Martin A. Gren, Göran Wahnström, Wetting of surfaces and grain boundaries in cemented carbides and the effect from local chemistry, Materialia 8 (2019), 100470.

[11] Z. Peng Fan, Zak Fang, Jun Guo, A review of liquid phase migration and methods for fabrication of functionally graded cemented tungsten carbide, Int. J. Refract. Met. Hard Mater. 36 (2013) 2–9.

[12] Peng Fan, Jun Guo, Zhigang Zak Fang, Paul Prichard, Design of cobalt gradient via controlling carbon content and WC grain size in liquid-phase-sintered WC–co composite, Int. J. Refract. Met. Hard Mater. 27 (2) (2009) 256–260.

[13] Peng Fan, Zhigang Zak Fang, H.Y. Sohn, Mathematical modeling of liquid phase migration in solid–liquid mixtures: application to the sintering of functionally graded WC–co composites, Acta Mater. 55 (9) (2007) 3111–3119.

[14] Axel Bjerke, Binder Migration in Double Pressed Drill Bit Inserts, Master's thesis, Department of physics, division of solid state physics, Lund university, 2018.

[15] A.A. Matveichuk, S.A. Davidenko, On the interaction of the cobalt melt with polycrystalline tungsten monocarbide, J. Superhard Mater. 40 (3) (2018) 184–188.

[16] Kaiming Cheng, Xu Tao, Hao Zhang, Shaoqing Wang, Du Yong, Lijun Zhang, Defang Kong, Zhongjian Zhang, Application of CALPHAD approach in simulation of liquid phase migration of cellular cemented carbide, Int. J. Refract. Met. Hard Mater. 42 (2014) 180–184.

[17] A.F. Lisovsky, Thermodynamics of the formation of composite material structures. A review, J. Superhard Mater. 37 (6) (2015) 363–374.

[18] A.F. Lisovsky, On the formation of a refractory skeleton in composite materials. A review, J. Superhard Mater. 35 (2) (2013) 65–76.

[19] A.F. Lisovsky, N.A. Bondarenko, The role of interphase and contact surfaces in the formations of structures and properties of diamond-(WC-co) composites. A review, J. Superhard Mater. 36 (3) (2014) 145–155.

[20] A.F. Lisovsky, Thermodynamics of a new phase formation in a composite material, J. Superhard Mater. 38 (4) (2016) 230–234.

[21] A.F. Lisovskii, Thermodynamics of sintering composite materials with the liquid phase present, J. Superhard Mater. 33 (3) (2011) 166–172.

[22] A.F. Lisovsky, Thermodynamics of the nanoparticle consolidation, Sci. Sinter. 41 (1) (2009) 3–10.

[23] Henrik Larsson, The yapfi phase-field implementation, in: arXiv preprint arXiv: 2104.11501, 2021.

[24] J.-O. Andersson, Thomas Helander, Lars Höglund, Pingfang Shi, Bo Sundman, Thermo-calc & DICTRA, computational tools for materials science, Calphad 26 (2) (2002) 273–312.

[25] Malin Mårtensson, Susanne Norgren, Impact of chromium on the magnetic properties of wc-co hardmetals, in: European Congress and Exhibition on Powder Metallurgy. European PM Conference Proceedings, The European Powder Metallurgy Association, 2016, pp. 1–7.

[26] B. Jansson, J. Qvick, On the saturation magnetization of cemented carbides containing cubic carbides. plansee seminar, 2005.

[27] Thermo-Calc Software, Thermo-Calc Software Tcfe Steels/Fe-Alloys Thermodynamic Database Version 9, Accessed 8-2-2020, 2019.

[28] Emil Heyn, Short reports from the metallurgical and metallographical laboratory of the royal mechanical and technical testing institute of charlottenburg, Metallographist 5 (1903) 39–64.

[29] H.E. Exner, H. Fischmeister, Structure of sintered tungsten carbide–cobalt alloys, Arch. Eisenhuettenw. 37 (1966), 409–15 (May 1966).

[30] Pentronic, Pentroninc manufacturer of industrial temperature sensors and equipment for temperature measurement in industry, research and development. https://www.pentronic.se/, 2022. Accessed: 2022-11-30.

[31] Joseph I. Goldstein, Dale E. Newbury, Joseph R. Michael, Nicholas W.M. Ritchie, John Henry J. Scott, David C. Joy, Scanning Electron Microscopy and X-Ray Microanalysis, Springer, 2017.

[32] Jianxin Liu, Zhigang Zak Fang, Quantitative characterization of microstructures of liquid-phase-sintered two-phase materials, Metall. Mater. Trans. A 35 (6) (2004) 1881–1888.

[33] B. Roebuck, E.G. Bennett, Phase size distribution in WC/co hardmetal, Metallography 19 (1) (1986) 27–47.

[34] V.T. Golovchan, N.V. Litoshenko, On the contiguity of carbide phase in WC–co hardmetals, Int. J. Refract. Met. Hard Mater. 21 (5) (2003) 241–244.

[35] K.G. Stjernberg, Some relations between the structure and mechanical properties of WC–TiC–co alloys, Powder Metall. 13 (25) (1970) 1–12.

[36] Cyril Stanley Smith, Lester Guttman, Measurement of internal boundaries in three-dimensional structures by random sectioning, Trans. AIME 197 (1) (1953) 81–87.

[37] Henrik Larsson, Anders Engström, A homogenization approach to diffusion simulations applied to α+γ Fe–Cr–Ni diffusion couples, Acta Mater. 54 (9) (2006) 2431–2439.

[38] Henrik Larsson, Lars Höglund, Multiphase diffusion simulations in 1d using the DICTRA homogenization model, Calphad 33 (3) (2009) 495–501.

[39] Jan-Olof Andersson, John Ågren, Models for numerical treatment of multicomponent diffusion in simple phases, J. Appl. Phys. 72 (4) (1992) 1350–1355.

[40] José García, Sven Englund, Fredrik Haglöf, Controlling cobalt capping in sintering process of cermets, Int. J. Refract. Met. Hard Mater. 62 (2017) 126–133.

[41] Sven Englund, Controlling Co-Capping in Sintering of Cermets, Master's thesis,, Uppsala University, 2013.

[42] Lina Berglund, The Effect of Cooling Rate on Sintered Cemented Carbides, Master's thesis,, KTH royal institute of technology, 2020.